Biointerphases
A Journal of Biomaterials and Biological Interfaces

Anodic biofilms as the interphase for electroactive bacterial growth on carbon veil

Kateryna Artyushkova, Dan Roizman, Carlo Santoro, Lucinda Elizabeth Doyle, Abeed Fatima Mohidin, Plamen Atanassov, and Enrico Marsili

Citation: Biointerphases **11**, 031013 (2016); doi: 10.1116/1.4962264
View online: http://dx.doi.org/10.1116/1.4962264
View Table of Contents: http://scitation.aip.org/content/avs/journal/bip/11/3?ver=pdfcov
Published by the AVS: Science & Technology of Materials, Interfaces, and Processing

Anodic biofilms as the interphase for electroactive bacterial growth on carbon veil

Kateryna Artyushkova[a)]
Department of Chemical and Biological Engineering, Center for Micro-Engineered Materials (CMEM), University of New Mexico, Albuquerque, New Mexico 87131

Dan Roizman[a)]
Singapore Centre for Environmental Life Sciences Engineering (SCELSE), Nanyang Technological University, 60 Nanyang Drive, Singapore 637551 and Interdisciplinary Graduate School, Nanyang Technological University, Singapore 639798

Carlo Santoro[a),b)]
Singapore Centre for Environmental Life Sciences Engineering (SCELSE), Nanyang Technological University, 60 Nanyang Drive, Singapore 637551

Lucinda Elizabeth Doyle
Singapore Centre for Environmental Life Sciences Engineering (SCELSE), Nanyang Technological University, 60 Nanyang Drive, Singapore 637551 and Interdisciplinary Graduate School, Nanyang Technological University, Singapore 639798

Abeed Fatima Mohidin
Singapore Centre for Environmental Life Sciences Engineering (SCELSE), Nanyang Technological University, 60 Nanyang Drive, Singapore 637551

Plamen Atanassov
Department of Chemical and Biological Engineering, Center for Micro-Engineered Materials (CMEM), University of New Mexico, Albuquerque, New Mexico 87131

Enrico Marsili[c)]
Singapore Centre for Environmental Life Sciences Engineering (SCELSE), Nanyang Technological University, 60 Nanyang Drive, Singapore 637551 and School of Chemical and Biomedical Engineering, 62 Nanyang Drive, Singapore 637459

(Received 4 May 2016; accepted 24 August 2016; published 8 September 2016)

The structure and activity of electrochemically active biofilms (EABs) are usually investigated on flat electrodes. However, real world applications such as wastewater treatment and bioelectrosynthesis require tridimensional electrodes to increase surface area and facilitate EAB attachment. The structure and activity of thick EABs grown on high surface area electrodes are difficult to characterize with electrochemical and microscopy methods. Here, the authors adopt a stacked electrode configuration to simulate the high surface and the tridimensional structure of an electrode for large-scale EAB applications. Each layer of the stacked electrode is independently characterized using confocal laser scanning microscopy (CLSM) and digital image processing. *Shewanella oneidensis* MR-1 biofilm on stacked carbon veil electrodes is grown under constant oxidative potentials (0, +200, and +400 mV versus Ag/AgCl) until a stable current output is obtained. The textural, aerial, and volumetric parameters extracted from CLSM images allow tracking of the evolution of morphological properties within the stacked electrodes. The electrode layers facing the bulk liquid show higher biovolumes compared with the inner layer of the stack. The electrochemical performance of *S. oneidensis* MR-1 is directly linked to the overall biofilm volume as well as connectivity between cell clusters. © *2016 American Vacuum Society*. [http://dx.doi.org/10.1116/1.4962264]

I. INTRODUCTION

Bioelectrochemical systems (BESs) show promise for bioremediation of organics and metals, in addition to bioelectrosynthesis of high-value products.[1] In a BES, electrochemical reactions are catalyzed/mediated by microorganisms at ambient temperature and circumneutral *p*H.[2–5]

Microorganisms adapted to both anodic and cathodic conditions, where oxidation and reduction reactions are carried out, respectively, have been studied. Anodophilic microorganisms oxidize organic substrates, transferring electrons to the anode.[6–8] More recently, cathodophilic microorganisms that transfer electrons from the cathode to reduce terminal electron acceptors (e.g., oxygen, nitrate, sulfate, etc.) have been observed.[9–12]

[a)]K. Artyushkova, D. Roizman, and C. Santoro contributed equally to this work.
[b)]Author to whom correspondence should be addressed; electronic mail: carlo.santoro830@gmail.com. Present address: Department of Chemical and Biological Engineering, Center for Micro-Engineered Materials (CMEM), University of New Mexico, Albuquerque, New Mexico 87131.
[c)]Electronic mail: emarsili@ntu.edu.sg

Numerous anode materials, including stainless steel,[13–15] carbonaceous materials,[16–18] and other metals,[19] have been studied for BES application. The most utilized anodic materials are based on tridimensional (3D) carbonaceous materials.[20–34] Such materials are cheap, resistant to corrosion, environmentally friendly, and possess good mechanical strength and electrical conductivity.[20–34] Furthermore, 3D carbonaceous materials have a high surface area/volume ratio, which allows electrical interaction between the bacteria and electrode and increases electron transfer rate per unit of the geometric surface.[20] Examples include carbon brush,[21,22] carbon cloth,[23,24] carbon paper,[25,26] carbon felt,[27–29] and carbon veil (CV).[30–34]

Carbon brush has the highest surface area/volume ratio, which can be fully colonized by bacteria. However, the fibers are connected to a titanium core that increases the cost of electrodes substantially.[35] Carbon cloth and carbon paper have high electrical conductivity and are ideal for flat plate BESs.[36,37] Unfortunately, both materials do not have a high surface area/volume ratio and are fragile and not suitable for practical applications. Carbon felt is commonly used since it provides a compromise between the surface area/volume ratio and porosity, which results in superior electrical interaction between the electrode surface and electrochemically active biofilm (EAB). Because of the large pore size, the majority of the surface can be colonized by bacteria, even in thick electrodes. The current output on carbon felt is higher than that of the flat graphite sheet, but it does not increase proportionally with the surface area, indicating that other factors (e.g., diffusional limitations) are affecting the electron transfer process.[38] CV is used as an anode material because of its flexibility, low cost, high porosity, and high mechanical strength. CV can be wrapped in a complex geometry to increase the surface area/volume ratio, particularly for microbial fuel cells (MFC) applications.[39–42] The high porosity still guarantees rapid reagent/product diffusion to and from the material, and it has been tested in long-term applications with successful results.[43,44] Several such experiments using CV as anode in BESs have been already published.[39–44]

While carbonaceous materials offer great advantages in terms of current output and easy electrode fabrication, it is difficult to image the EAB grown on these 3D materials, due to technical limitations. Current microscopic and spectroscopic techniques are able to characterize: (1) (only) the very top surface of the biofilm;[38,45–47] (2) relatively thick biofilm only if the surface on which it was grown is transparent for laser;[48] (3) biofilm within 3D structure only if the density of the biofilm is different from the electrode surface.[49,50] There is no single microscopic or spectroscopic technique that provides full characterization of the thick biofilms on 3D carbonaceous materials. To overcome these limitations, a combination of existing techniques is often used.

Currently, several techniques are used to image EABs in BESs. The combination of multiple techniques provides an enhanced understanding of the biofilm structure and function, overcoming the limitations of a single characterization method. The main challenge is the characterization of EABs grown on structured materials with 3D features, such as those used in real-world applications of BESs. For example, digital pictures or video collected through CCD camera provide a low-cost characterization of the whole biofilm formation process, but they do not offer sufficient resolution to understand the details of the biofilm structure, particularly the thin biofilms associated with BESs, and cannot provide insight on the electrochemical aspect of the process.[51] Scanning electron microscopy (SEM) offers high-resolution details of the biofilm surface. However, electrons do not penetrate beyond the biofilm surface, and the sample pretreatments (drying and gold deposition under vacuum conditions) alter the biofilm structure and morphology.[52] When coupled with energy-dispersive x-ray spectroscopy (EDX), SEM enables visualization of the surface chemistry of the biofilms, thus identification of precipitates and biomass. However, SEM or EDX do not provide direct imaging of the redox activity of the biofilms. The environmental SEM allows imaging of the hydrated biofilms but only on the biofilm's outer surface, thus is not suitable for imaging of the structured biofilms on complex electrodes.[53] Recently, tomography (microCT) has been used for biofilm imaging on the cathode of a working MFC after six months of operation.[49] MicroCT can be used to image thick biofilms grown on complex electrodes and allows inorganic materials to be distinguished from organic and biological materials, due to the diversity of the various material densities.[54,55] The resolution at the electrode/biofilm interface is not as good as in SEM and does not allow visualization of single bacterial cells. However, microCT allows imaging of biofilm samples on electrodes without any pretreatment, thus maintaining the integrity of the biofilm morphology. High-resolution microCT, currently under development, is expected to contribute to high-quality imaging of biofilms.[55] Blanchet *et al.*[50] recently used 3D epifluorescent microscopy to investigate cross-sections of 3D carbon felt showing that a thick biofilm was formed on the external surface of the electrode after almost 40 days operation, but only 8%–32% of the total electrode was colonized, indicating that the fibers at the center of the electrode were poorly colonized or not colonized at all.

Confocal resonant Raman analysis[46,56,57] has been incorporated into previous studies. However, the methodology is complex and not suitable for routine characterization of 3D electrode materials. Visible spectroelectrochemistry offers good insight into the electron transfer mechanisms in biofilms,[58] but its application is limited to very thin EABs.

X-ray photoelectron spectroscopy (XPS) is a surface analytical spectroscopic method that provides an elemental and chemical composition of the biofilm within the very top surface of the material.[59,60] The main limitations of XPS for analysis of the biofilm on 3D electrode surfaces are (1) signal is limited to the top ~5–10 nm of the biofilm, (2) low spatial resolution of images in comparison with other methods, and (3) vacuum incompatibility of the biofilm samples, requiring either drying the biofilm, thereby affecting its

chemistry and morphology, or freeze-drying which are experiments beyond routine use. With the development of new ion sources for depth profiling of organic and biological materials and the improvement in spatial resolution, imaging cryo-XPS combined with ion beam sputtering of the material has the potential for providing chemical spatially resolved information in three dimensions, albeit at the price of very long experiment times.

Confocal laser scanning microscopy (CLSM) is by far the most utilized nondestructive method for biofilm imaging.[52,61,62] The main advantages are based on the possibility of imaging with minimal or no pretreatment and on the very high image resolution that can be in the range of 100 nm, enabling the distinction of a single bacterium. Unfortunately, the higher the image quality and scanning resolution, the smallest the area imaged and longer the time is for image collection, which affects the biofilm formed on the surfaces.[62,63] The main problems are related to biofilm thickness and 3D surfaces. In fact, CLSM photons can only penetrate thicknesses less than 0.5 mm, while for thicker biofilms, this technology cannot be used accurately. Moreover, CLSM photons can penetrate semitransparent matters (e.g., biofilm) but are stopped by nontransparent matter like inorganic fouling or carbon fibers.

The morphology of *Shewanella oneidensis* EAB grown on transparent self-assembled monolayers (SAMs) was previously studied through CLSM in combination with quantitative image analysis.[47] In the current study, we extend this approach for EABs grown on fibrous 3D carbonaceous materials under different applied potentials. Here, *S. oneidensis* MR-1 was chosen as a model EAB-forming microorganism due to its ability to transfer electrons via both anodic and cathodic extracellular electron transfer (EET).[64] Thin CV was used as the anode material, and eight layers were overlapped to create a complex 3D carbonaceous electrode. The two outer layers and the middle layer #4 were then analyzed separately using CLSM to determine the biofilm's microstructure.

II. MATERIALS

A. Electrochemical cell assembly

Pyrex bottles of 100 ml volume were fitted with CV working electrode, titanium (Ti) coil counter electrode, and Ag/AgCl reference electrodes (Fig. 1). A salt bridge composed of 1 M KCl mixed with 1.5% autoclaved agar and topped with liquid 1 M KCl was used to avoid microbial contamination and maintain ionic conductivity. The salt bridge was inserted into a glass tube ($\Phi = 4$ mm) ending with a vycor glass frit. The working electrode consisted of CV (Alfa Aesar, 0.5 mm thick, 99%) with a geometric area of 2 $\times$ 1 cm^2. Eight pieces of CV were overlapped and attached to a Ti wire through a nylon screw and nut to ensure electrical contact. The bottles were then sealed with epoxy resin to minimize oxygen concentration during microbial growth (Fig. 1). During the experiments, ultrahigh purity nitrogen was flushed to preserve anaerobic conditions. The electrolyte was continuously stirred using a magnetic stirring bar. All the experiments were carried out at room temperature. Prior to electrochemical experiments, *S. oneidensis* MR-1 was grown overnight in lysogeny broth medium at room temperature under shaking conditions of 150 rpm, to an optical density OD_{600} of 1.6–1.7, measured with a UV-visible spectrophotometer (Shimadzu, Japan) and inoculated to an optical density at 600 nm (OD_{600}) of 1.6–1.7 as measured with a UV-visible spectrophotometer. During electrochemical experiments, bacterial cultures were grown in modified M1 medium (*p*H 7.2) containing 20 mM lactate, 7.5 mM NaOH, 30 mM 4-(2-hydroxyethyl)-1-piperazineethanesulfonic acid), 28.04 mM NH_4Cl, 1.34 mM KCl, 4.35 mM NaH_2PO_4, 0.68 mM $CaCl_2$, and supplemented with trace vitamins and minerals.[65]

B. Electrochemical analysis

The electrochemical cells were connected to a multichannel VSP potentiostat (Bio-Logic, France). The potential of the working electrode was set at 0, 200, or 400 mV versus Ag/AgCl for the whole experiment. Eight independent

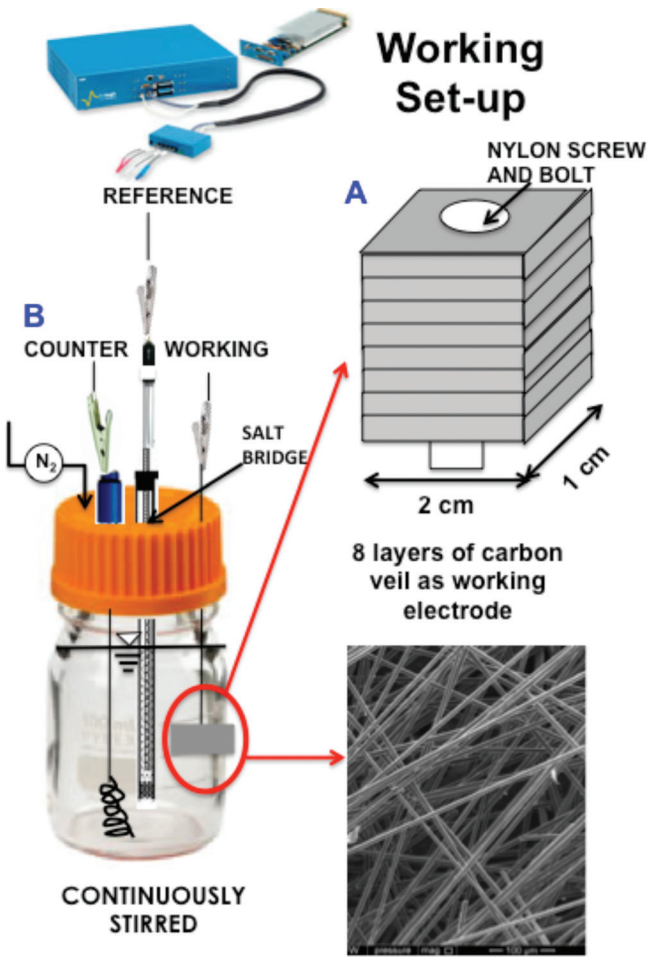

FIG. 1. Experimental setup. The eight CV electrodes were attached via a nylon screw and bolt (a) and placed in a horizontal position inside a 100 ml glass bottle fitted with a Ti coil counter electrode and an Ag/AgCl reference electrode attached to a salt bridge (b).

biological experiments for each working potential were carried out. During the electrochemical tests, three "sacrificial" cells were opened for CLSM imaging purposes at 16, 45, and 65 h, respectively. At least two cells for each potential were run for over 180 h (7.5 days). Before CLSM imaging, the eight CV layers were carefully disassembled, and the two outer layers and the middle layer #4 were selected.

C. CLSM imaging

The biofilms were stained with Molecular Probes (now Thermo Fisher) LIVE/DEAD® BacLight™ as described by the manufacturer with additional modifications, to account for the CV substrate;[66] briefly, each sampled piece of CV was carefully removed using sterile tweezers, washed in 20 ml of phosphate buffered saline (PBS) containing 137 mM NaCl, 2.7 mM KCl, 10 mM Na_2HPO_4, 1.8 mM KH_2PO_4, 1 mM $CaCl_2$, and 0.5 mM $MgCl_2$ (pH = 7.2) for 5 min. Following the wash, samples were carefully placed in a 2 ml Eppendorf tube containing 1 ml of PBS supplemented with 1.5 μl of each dye: SYTO® 9 and propidium iodide, and stained for 30 min. This stain allowed viable bacteria, with intact plasma membranes, to be distinguished from dead bacteria, with compromised membranes. After staining, samples were washed again to remove unbound dye and reduce background noise and placed on a standard glass slide covered with 0.21 mm standard glass coverslip and sealed with nail polish. Three-dimensional confocal images were collected with a ZEISS 780 inverted CLSM using a 40× Plan-Apochromat Korr lens, NA = 0.95. Three random locations were chosen for each CV sample at each time point. A Z-stack acquisition strategy was chosen, with an area of 212 × 212 μm being imaged on an XY plane. Twenty six planes were stacked, with 3 μm distance, covering a depth of about 80 μm for each location. We employed three channels: (1) channel 1 for Syto9 (green) live stain; excitation = 488 nm, emission = 500–583 nm; (2) channel 2 for propidium iodide (red) dead stain; excitation = 561 nm, emission = 567–719 nm; and (3) channel 3 using the onboard transmitted photomultiplier tube, for viewing the surface of the CV (appearing as dark, in contrast to the bright background).

D. Image processing

Digital image processing was done using the graphical user interface (GUI) in MATLAB. An in-house written GUI for image processing is available at the Mathworks File Exchange website at http://goo.gl/IHavd6.[67]

The following volumetric, textural, and aerial parameters were calculated: (1) biovolume, which is measured as the total number of pixels where biomass is present; (2) biofilm cluster size, measured as the number of consecutive biomass pixels representing clusters in a given direction. Only the cluster size in the x-direction was included in results, as the trends in evolution of cluster sizes in all three directions (x, y, and z) were identical; 1 pixel is equivalent to ~5 linear micrometer; (3) uniformity, representing the homogeneity or orderliness of the image; (4) entropy, measuring the degree of randomness, with more complex and more heterogeneous images having higher entropy (which increases with the number of biofilm clusters); (5) porosity, i.e., the ratio of empty pixels (without the biofilm) to the total volume; and (6) connectivity of biofilm clusters, measured as Euler number. Euler number is the total number of cells minus the total number of pores in the image. The lower the Euler number, the higher the connectivity.

III. RESULTS AND DISCUSSION

A. Electrochemical output

The current output for *S. oneidensis* MR-1 at 0, +200, and +400 mV versus Ag/AgCl is shown in Fig. 2. The current density for the electrodes polarized at 0 mV (versus Ag/AgCl) increased rapidly to a maximum of 17 ± 2 μA cm^{-2}, then it decreased gradually to 15 ± 3 μA cm^{-2}. The electrodes poised at 200 mV versus Ag/AgCl increased to 7 ± 2 μA cm^{-2}, and then, the current density dropped to 5 ± 1 μA cm^{-2} and remained stable until the end of the experiment. The electrodes maintained at +400 mV (versus Ag/AgCl) rapidly reached a very high value of 16 ± 4 μA cm^{-2}, and then, the current density dropped to 5 ± 1 μA cm^{-2} and remained stable until the end of the experiment. The rapid decrease of current density for the electrode poised at +400 mV (versus Ag/AgCl) may be due to the oxidative damage of membrane cytochromes as recently shown.[68] However, the results at +200 mV (versus Ag/AgCl) suggest that other limitations, possibly due to the rapid growth of the biofilms and the consequent rapid consumption of nutrients in the outer layer of the biofilms and diffusional limitations of the substrate, play a role in the sudden decrease of the current density output.

B. Imaging output

The confocal images extend 90 μm within the biofilms, including part of the CV electrode [+400 mV (versus Ag/AgCl), Fig. 3], due to the high porosity and low fiber diameter of the electrode material. Most of the cells were alive immediately after sampling, indicating the nonlimiting

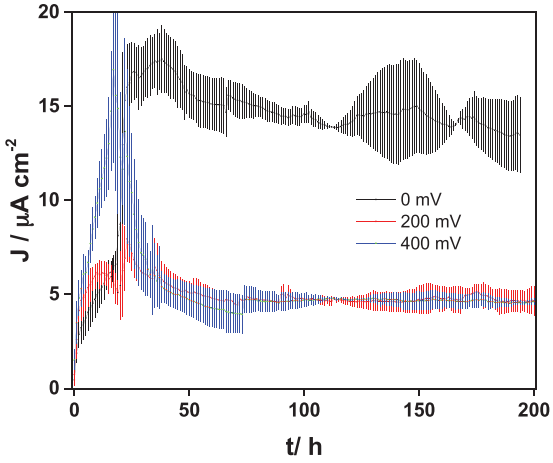

FIG. 2. Current density at various applied potentials with error bars.

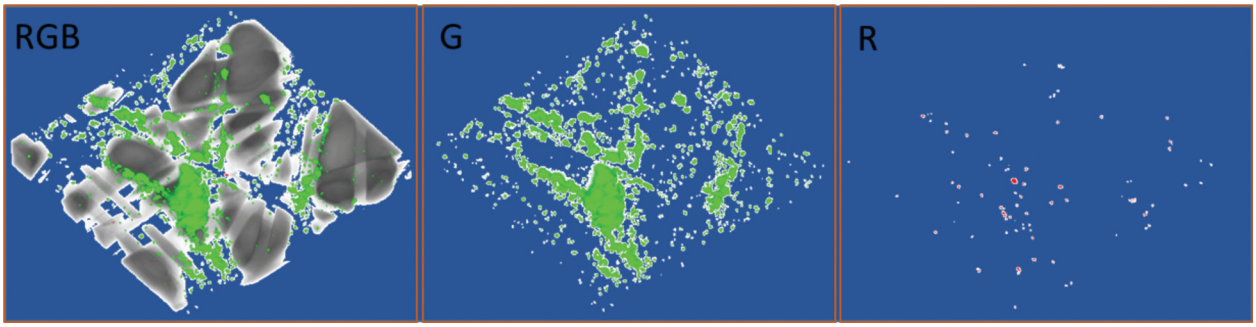

FIG. 3. Three-dimensional confocal volumes at +400 mV, where gray represents the electrode fibers, the green channel captures live biofilm, and the red channel registers dead cells.

diffusion of the substrate within the biofilm. The cells were mainly arranged around the fibers. The choice of low OD (≈0.1) of the inoculum was to avoid a thick biofilm on the fibers, thus allowing imaging through the fibers and hence a 3D characterization of the biofilm.

The biofilms grew rapidly on the electrode, with an extensive coverage after 45 h (Fig. 4). The visual analysis shows the presence of larger cells clustered on the bottom electrode layer while the top layers showed a more homogeneous biofilm distribution. The quantitative biofilm image analysis was calculated from CLSM images acquired at +400 mV (versus Ag/AgCl) from the top, middle, and bottom part of the biofilm after 16 h (day 1), 45 h (day 2), and 65 h (day 3). Figure 5(a) shows the workflow of volumetric image analysis: (1) the 3D image stack was acquired; and (2) the volume was thresholded to identify cell clusters and to calculate biovolume, porosity, and average run length. The textural parameters described below (e.g., entropy and uniformity) were calculated from the gray scale intensity volumes in Fig. 5(b).

A set of volumetric and aerial metrics derived from binary volumes was first calculated, with all pixels having a fluorescent intensity above a certain value due to live cells assigned the value of 0 (black), and the rest assigned a value of 1 (white).[61,62] For consistency among all datasets, the same value was chosen for thresholding images to black and

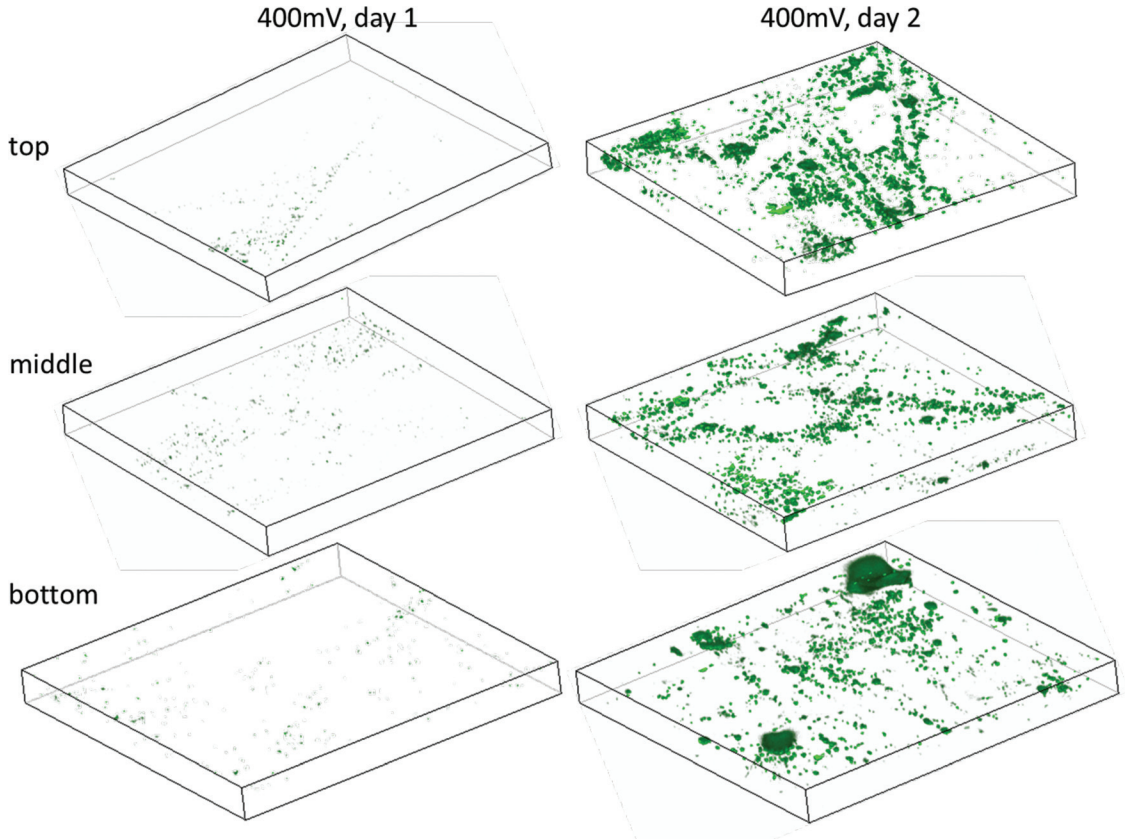

FIG. 4. Three-dimensional confocal volumes of the green channel at +400 mV (live cells) for the top, middle, and bottom layers of the electrode after 16 h (left) and after 45 h (right).

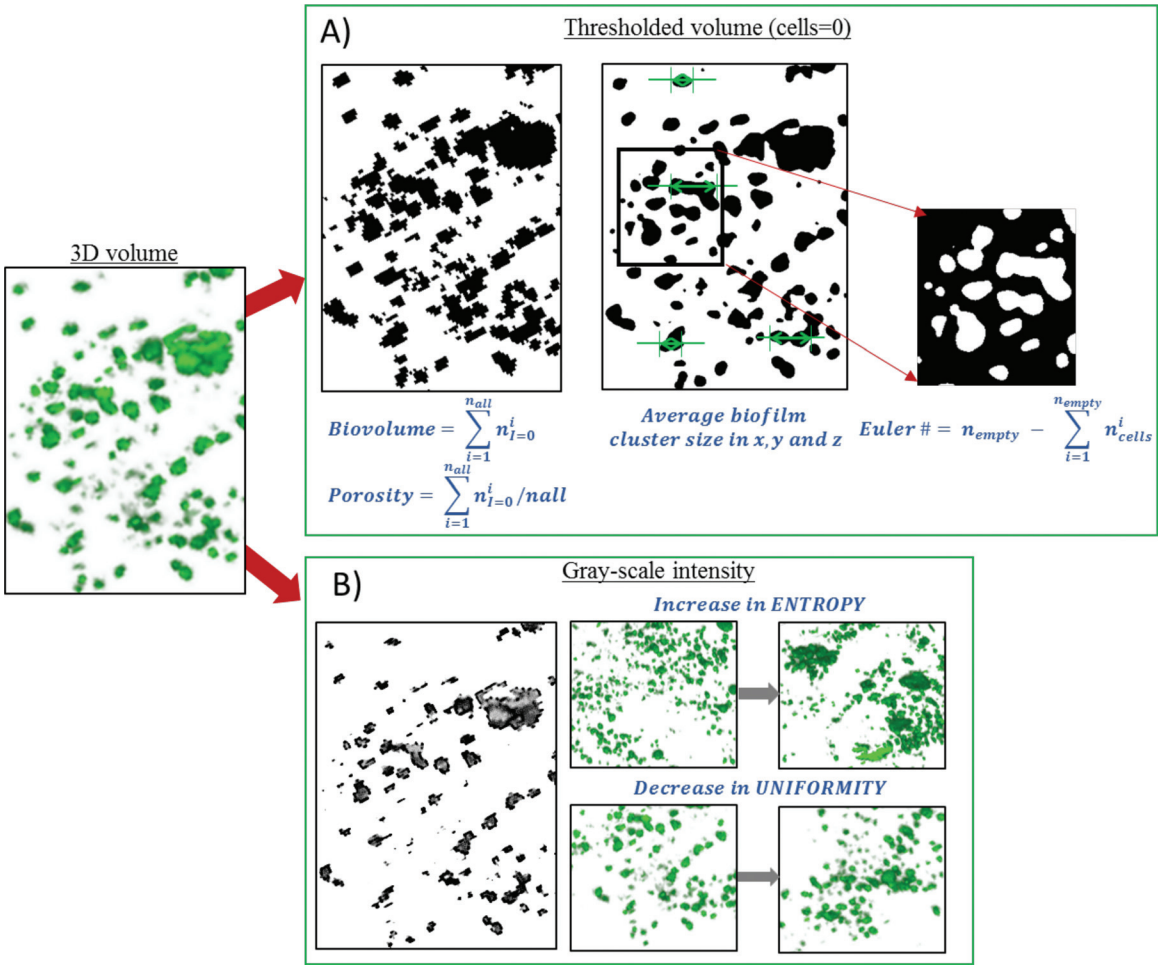

FIG. 5. Metrics calculations from 3D volumes. (a) Aerial and volumetric metrics is calculated from thresholded images. (b) Texture characteristics are computed from gray scale intensity using GLCM.

white. From these binary volumes, we calculated *biovolume*, which is the total number of pixels within the volume having a value of 0 due to present bacteria, and *porosity* which is the ratio of pixels having a value of 1, i.e., where no bacteria are present, to the total number of pixels. Physical dimensions of biofilm clusters were expressed as *the average run length* which is the average number of consecutive biomass pixels representing cell clusters in a given direction (x, y, and z) in the 3D volume. *Euler number* is an important topological characteristic that is related to connectivity of the biofilm formed.[69] The definition of Euler number is the total number of objects in the image minus the total number of holes in the image. For the Euler number to represent connectivity of the biofilm, images were inverted so that cells (objects) are treated as connected sets of pixels that have a value of 1 while holes are the empty areas between the cells. The smaller the Euler number, the more connected the biofilm is.

The second set of metrics is derived from the grayscale intensity is texture parameters. The texture parameters represent the spatial relationship of pixels by calculating the gray-level co-occurrence matrix (GLCM). GLCM is a matrix that represents how often pairs of a pixel in a specified spatial relationship with specific values occur in an image, from which statistical measures such as contrast, homogeneity, entropy, and uniformity can be extracted. The first parameter is *textural entropy* which measures the degree of randomness in the image. The increase in a number of cell clusters due to growth results in more complex textures and more heterogeneous images as shown in the example in Fig. 6, which is reflected in higher entropy. *Uniformity* (also known as inverse difference moment) of the image is related to the orderliness of the structure and is sensitive to change in disorder. Heterogeneous images with fewer repeated patterns have lower uniformity, while frequent and repeated patterns of pixel clusters, as shown in the example, result in higher uniformity.

Heterogeneity of the biofilm is evident from the extracted metrics such as biofilm volumes for the top, middle, and bottom layers of the electrode as a function of time in Fig. 6. A large spread of values indicates that it is important to look at the biofilm properties from all three regions.

Metrics discussed in Sec. II were calculated from 3D confocal volumes of the top, middle, and bottom layers of the 3D electrode. It is important to remember that both top and bottom layers of the electrode are facing the bulk solution

	day 1	day 2	day 3
Top	93321	621921	1007583
Middle	165022	392138	427133
Bottom	49736	901691	715324

FIG. 6. Biovolumes in a number of pixels for the top, middle, and bottom layers of the electrode as a function of time after inoculation. The sensitivity of the biovolume measurement is ~25 000 pixels.

while the middle layer of the electrode may have limited contact with nutrients resulting in a different formation and development of the biofilm. The EET rate may be affected by the properties of the superficial biofilm but to a smaller extent than the biofilm in direct contact with the solution due to limited diffusion of nutrients in the deeper part of the biofilm.[70]

At 0 mV (versus Ag/AgCl), the morphological properties of the biofilm grown are depicted in Fig. 7. The total amount of biofilm is lower than on the electrode polarized at +200 and +400 mV (versus Ag/AgCl). The biofilm in the middle CV layer polarized at 0 mV indeed shows different morphological properties from the outer layers. In the outer layers, cell cluster size grew rapidly from 3 to 5 pixels which corresponds to 15–25 μm and then decreased. In the middle of the biofilm, the cluster size decreases from 20 to 15 μm. The entropy and uniformity also decreased from day 1 to day 2, but then no textural changes were observed at the later time. Porosity changes inconsistently, likely due to a small amount of biofilm grown. The connectivity of the biofilm also did not change much. These temporal changes in the morphological properties indicate that at 0 mV (versus Ag/AgCl), the growth of the biofilm is slow with stable morphology observed. This is consistent with the stable current output, which decreased slowly after reaching its maximum value.

Figure 8 shows the evolution of the same metrics extracted from the biofilm grown on the electrodes poised at +200 mV (versus Ag/AgCl). Again, striking differences between the middle and outer layers of the electrode are observed. The outer layers have very similar temporal behavior and, even though, from day 1 to day 2, there is a significant growth of the biofilm with growing biofilm clusters (13–35 μm), increasing entropy, decreasing uniformity, and decreasing porosity, there is a dramatic loss of the biofilm on day 3—with biofilm volume, cell cluster size, and porosity all returning to the values at the beginning of biofilm growth. This is in good agreement with electrochemical data—instability of the biofilm causes low maximum current densities which are deteriorating with time.

Figure 9 shows evolution in morphological metrics as a function of time for the electrode poised at +400 mV (versus Ag/AgCl). The biofilm grown at this potential shows much higher uniformity in all layers analyzed. Trends in parameters from the top, middle, and bottom layers of the electrode are very similar. As the biofilms grew, viable biovolume also increased. At the same time, biofilm cluster size and entropy increased, due to the accumulation of cells into clusters. The growth of cell clusters from 2 to 9 μm is observed. This was also accompanied by a decrease in uniformity and porosity. The major change happened between 16 and 45 h after inoculation, with most of the morphological parameters remaining constant after that point. Correspondingly, the connectivity improved by the third day. The biofilm on the middle electrode layer lost connectivity after 65 h, likely because of biofilm dispersal. These parameters are consistent with high current densities, which, however, are not stable and drop at longer times of operation.

Figure 10 shows the relationship between biofilm properties extracted at all polarizations from the three CV layers as a function of current density obtained in Fig. 2 at relevant times of confocal observations. Biovolume, porosity, and Euler number (inverse of connectivity) are plotted as a

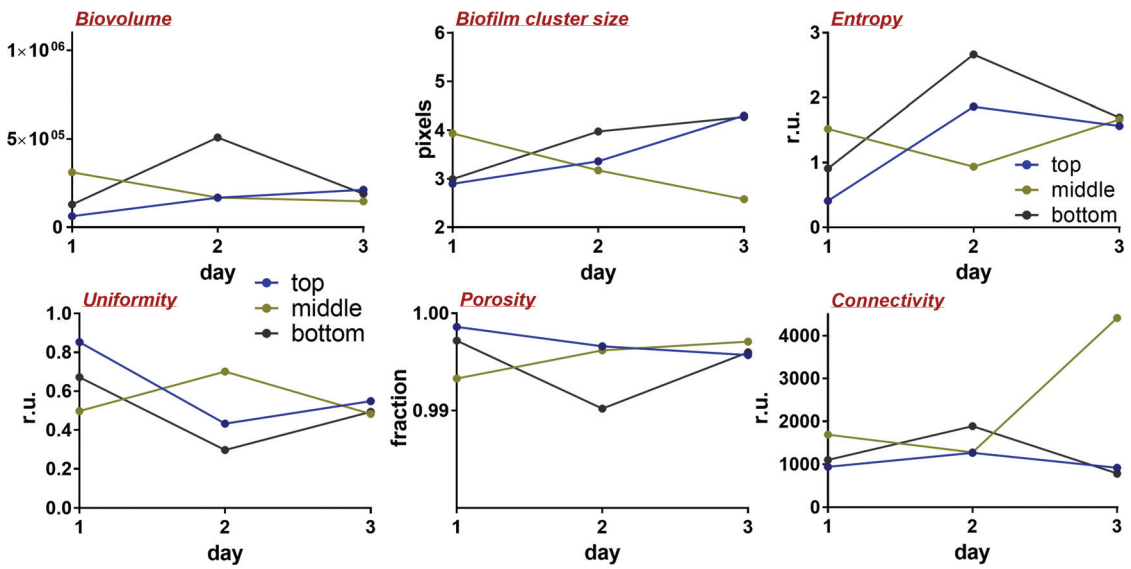

FIG. 7. Metrics extracted from 3D confocal volumes of the biofilm grown at 0 mV (vs Ag/AgCl).

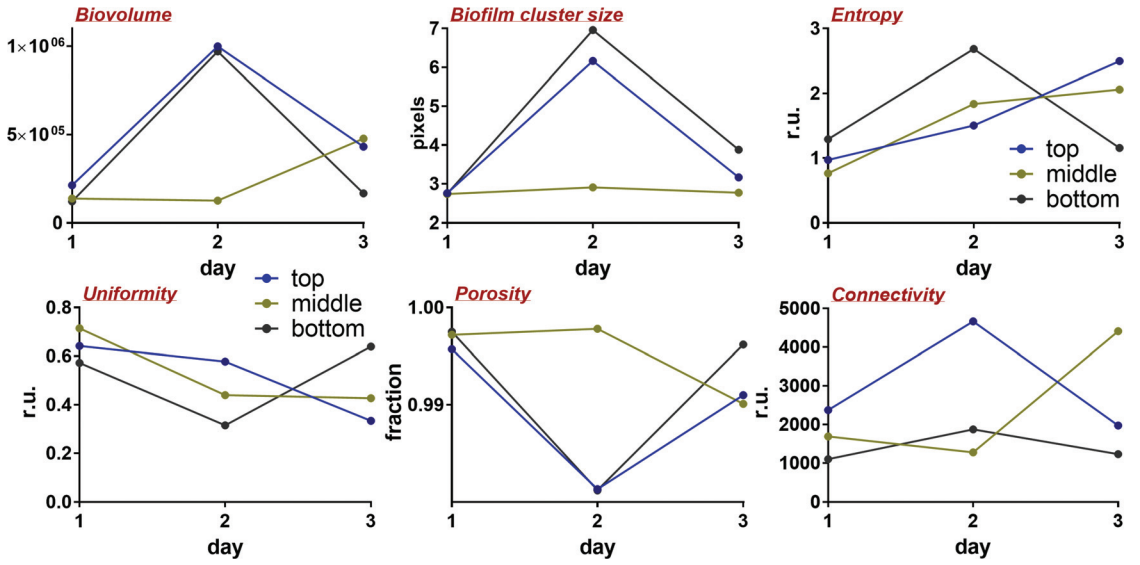

FIG. 8. Metrics extracted from 3D confocal volumes of the biofilm grown at +200 mV (vs Ag/AgCl).

function of current density. There are two clusters of metrics obtained: one corresponds to electrodes producing low current densities—between 4 and 6 μA cm^{-2} and the other corresponds to electrodes producing high current densities between 14 and 17 μA cm^{-2}. For poorly performing electrodes, the total viable biovolume, porosity, and connectivity of the biofilm have broad range of values as shown in Fig. 10. Importantly, the biofilms that produce highest current density have much smaller range of values of the morphological properties, which indicates good electrochemical performance. High connectivity, high porosity, and low biovolume are characteristic of the biofilms with high current densities. We have demonstrated for model SAM based system that thick biofilms are not beneficial for MFC operations and they create diffusional resistance to electron donor transport.[47] Connectivity between cell clusters was also shown to be critically important for facilitating electron transfer for the model SAM based grown biofilms. From these structure-to-property correlations, it is clear that the biofilms that do not have high biovolume of viable cells but have high connectivity between cell clusters result in higher current densities.

C. Outlook

To the best of our knowledge, this is the first time that CLSM images are used to characterize biofilm forming on a 3D carbonaceous material. Images were not taken along the entire thickness of the CV due to CLSM's limitations, but the high CV porosity and the low diameter of the fibers allowed penetration through the complex matrix for over 90 μm on each single CV layer. The choice of stacking the CV sheets and analyzing the top, bottom, and middle layers facilitated a better understanding of the dynamics of the

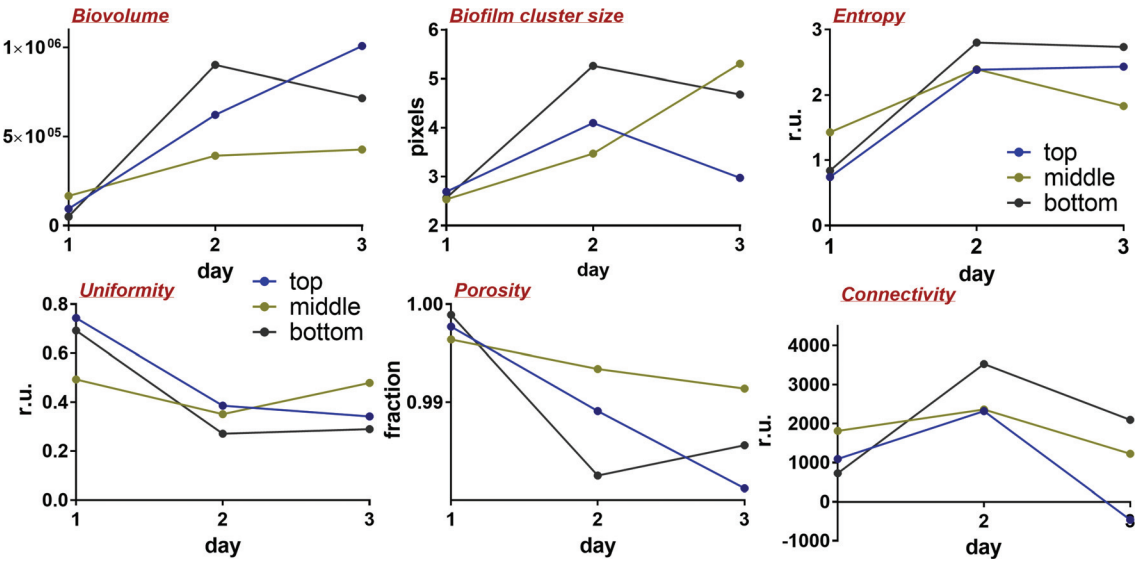

FIG. 9. Metrics extracted from 3D confocal volumes of the biofilm grown at +400 mV (vs Ag/AgCl).

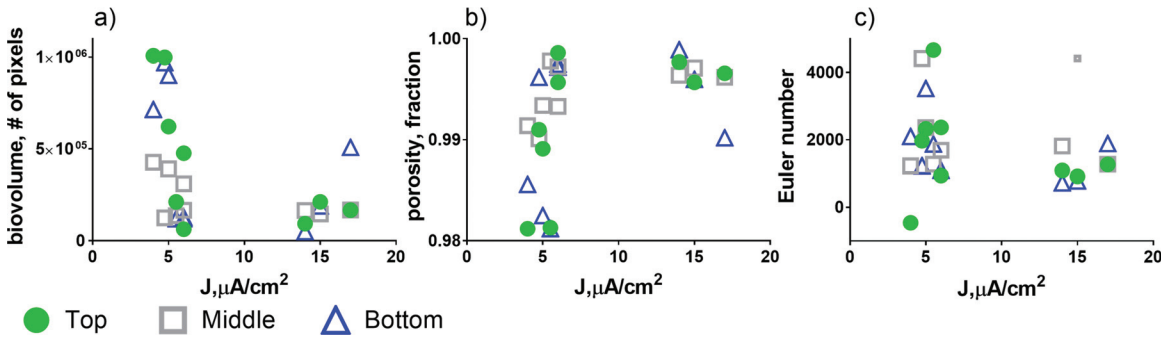

FIG. 10. Metrics extracted from 3D confocal volumes: (a) biovolume, (b) porosity, and (c) Euler number as a function of current density.

biofilm inside a complex 3D carbonaceous electrode. In general, the top and bottom CV layers had a higher biofilm formation due to the direct exposure of bacteria to the bulk solution. The middle CV layer had the smallest biofilm present in all regions tested (determined by biovolume), likely due to the low diffusion of substrate influenced by the tortuosity and complexity of the 3D carbonaceous electrode and the rapid consumption of nutrients in the outer layers of the biofilm.

IV. CONCLUSIONS

For the first time, we characterized *S. oneidensis* MR-1 biofilm microstructure on a complex 3D carbonaceous material, by stacking eight layers of CV, polarizing the overall electrode at different potentials (0, +200, and +400 mV versus Ag/AgCl) and subsequently monitoring biofilm formation and development on three different layers. Due to the existing limitations in imaging biofilm in a complex carbonaceous matrix, the top, middle, and bottom layers have been imaged separately using CLSM and digital image processing to provide relevant analysis of the biofilm structure. Several textural, aerial, and volumetric parameters have been calculated from the CLSM images, and the development of the biofilm properties has been presented. The biofilm formed showed large heterogeneity among the layers investigated. The biovolume increased with the operational time, and interestingly, the middle layer had a lower biovolume, indicating the difficulty of the biofilm to colonize the inner layers of the complex 3D electrodes. In parallel, biofilm cluster size and entropy increased, and uniformity and porosity decreased over time.

ACKNOWLEDGMENTS

The authors acknowledge financial support from Singapore Centre for Environmental Life Sciences Engineering (SCELSE), whose research was supported by National Research Foundation Singapore, Ministry of Education, Nanyang Technological University, and National University of Singapore, under its Research Centre of Excellence Program.

[1]F. Harnisch and U. Schröder, Chem Soc Rev. **39**, 4433 (2010).
[2]Y. A. Gorby *et al.*, Proc. Natl. Acad. Sci. U. S. A. **103**, 11358 (2006).
[3]C. Santoro, S. Babanova, K. Artyushkova, J. A. Cornejo, L. K. Ista, O. Bretschger, E. Marsili, P. Atanassov, and A. J. Schuler, Bioelectrochemistry **106**, 141 (2015).
[4]R. M. Snider, S. M. Strycharz-Glaven, S. D. Tsoi, J. S. Erickson, and L. M. Tender, Proc. Natl. Acad. Sci. U. S. A. **109**, 15467 (2012).
[5]D. R. Bond, S. M. Strycharz-Glaven, L. M. Tender, and C. I. Torres, ChemSusChem **5**, 1099 (2012).
[6]N. Lebedev, S. M. Strycharz-Glaven, and L. M. Tender, ChemPhysChem **15**, 320 (2014).
[7]S. M. Strycharz-Glaven, J. Roy, D. Boyd, R. Snider, J. S. Erickson, and L. M. Tender, ChemElectroChem **1**, 1957 (2014).
[8]M. D. Yates, J. P. Golden, J. Roy, S. M. Strycharz-Glaven, S. Tsoi, J. S. Erickson, M. Y. El-Naggar, S. Calabrese Barton, and L. M. Tender, Phys. Chem. Chem. Phys. **17**, 32564 (2015).
[9]Z. Wang *et al.*, Appl. Environ. Microbiol. **81**, 699 (2015).
[10]P. Cristiani, A. Franzetti, I. Gandolfi, E. Guerrini, and G. Bestetti, Int. Biodeterior. Biodegrad. **84**, 211 (2013).
[11]M. Daghio, I. Gandolfi, G. Bestetti, A. Franzetti, E. Guerrini, and P. Cristiani, New Biotechnol. **32**, 79 (2015).
[12]M. Rimboud, A. Bergel, and B. Erable, Bioelectrochemistry **110**, 46 (2016).
[13]E. Guerrini, P. Cristiani, M. Grattieri, C. Santoro, B. Li, and S. Trasatti, J. Electrochem. Soc. **161**, H62 (2014).
[14]S. F. Ketep, A. Bergel, A. Calmet, and B. Erable, Energy Environ. Sci. **7**, 1633 (2014).
[15]B. Erable, R. Lacroix, L. Etcheverry, D. Féron, M. L. Delia, and A. Bergel, Bioresour. Technol. **142**, 510 (2013).
[16]T. Schiliro', T. Tommasi, C. Armato, D. Hidalgo, D. Traversi, S. Bocchini, G. Gilli, and C. F. Pirri, Energy **106**, 277 (2016).
[17]S. Chen, G. He, X. Hu, M. Xie, S. Wang, D. Zeng, H. Hou, and U. Schröder, ChemSusChem **5**, 1059 (2012).
[18]J. Wei, P. Liang, and X. Huang, Bioresour. Technol. **102**, 9335 (2011).
[19]A. Baudler, I. Schmidt, M. Langner, A. Greiner, and U. Schröder, Energy Environ. Sci. **8**, 2048 (2015).
[20]K. Guo, A. Prévoteau, S. A. Patil, and K. Rabaey, Curr. Opin. Biotech. **33**, 149 (2015).
[21]B. Logan, S. Cheng, V. Watson, and G. Estadt, Environ. Sci. Technol. **41**, 3341 (2007).
[22]F. Soavi, L. G. Bettini, P. Piseri, P. Milani, C. Santoro, P. Atanassov, and C. Arbizzani, J. Power Sources **326**, 717 (2016).
[23]D. Pant, G. Van Bogaert, C. Porto-Carrero, L. Diels, and K. Vanbroekhoven, Water Sci. Technol. **63**, 2457 (2011).
[24]B. Li *et al.*, Electrochim. Acta **134**, 116 (2014).
[25]C. Santoro, M. Guilizzoni, J. P. Correa Baena, U. Pasaogullari, A. Casalegno, B. Li, S. Babanova, K. Artyushkova, and P. Atanassov, Carbon **67**, 128 (2014).
[26]Y.-R. He, X. Xiao, W.-W. Li, G.-P. Sheng, F.-F. Yan, H.-Q. Yu, H. Yuan, and L.-J. Wu, Phys. Chem. Chem. Phys. **14**, 9966 (2012).
[27]D. Hidalgo, T. Tommasi, S. Bocchini, A. Chiolerio, A. Chiodoni, I. Mazzarino, and B. Ruggeri, Energy **99**, 193 (2016).
[28]D. Hidalgo, A. Sacco, S. Hernández, and T. Tommasi, Bioresour. Technol. **195**, 139 (2015).
[29]Mustakeem, Mater. Renewable Sustainable Energy **4**, 22 (2015).
[30]J. Winfield, I. Ieropoulos, and J. Greenman, Bioresour. Technol. **110**, 245 (2012).

[31]P. Ledezma, J. Greenman, and I. Ieropoulos, Bioresour. Technol. **118**, 615 (2012).
[32]I. Gajda, J. Greenman, C. Melhuish, and I. Ieropoulos, Bioelectrochemistry **104**, 58 (2015).
[33]X. A. Walter, J. Greenman, and I. A. Ieropoulos, Bioresour. Technol. **172**, 365 (2014).
[34]I. A. Ieropoulos, J. Greenman, and C. Melhuish, Int. J. Hydrogen Energy **38**, 492 (2013).
[35]V. Lanas, Y. Ahn, and B. E. Logan, J. Power Sources **247**, 228 (2014).
[36]B. Min and B. E. Logan, Environ. Sci. Technol. **38**, 5809 (2004).
[37]S. Kazemi, K. Fatih, and M. Mohseni, Can. J. Chem. Eng. **93**, 479 (2015).
[38]M. Epifanio, S. Inguva, M. Kitching, J. P. Mosnier, and E. Marsili Bioelectrochemistry **106**, 186 (2015).
[39]I. Ieropoulos, J. Greenman, C. Melhuish, and I. Horsfield, ChemSusChem **5**, 1020 (2012).
[40]P. Ledezma, A. Stinchcombe, J. Greenman, and I. Ieropoulos, Phys. Chem. Chem. Phys. **15**, 2278 (2013).
[41]P. Ledezma, J. Greenman, and I. Ieropoulos, Bioresour. Technol. **134**, 158 (2013).
[42]G. Papaharalabos, J. Greenman, C. Melhuish, C. Santoro, P. Cristiani, B. Li, and I. Ieropoulos, Int. J. Hydrogen Energy **38**, 11552 (2013).
[43]I. Ieropoulos, J. Greenman, and C. Melhuish, Phys. Chem. Chem. Phys. **14**, 94 (2012).
[44]I. A. Ieropoulos, P. Ledezma, A. Stinchcombe, G. Papaharalabos, C. Melhuish, and J. Greenman, Phys. Chem. Chem. Phys. **15**, 15312 (2013).
[45]A. Jain, J. O. Connolly, R. Woolley, S. Krishnamurthy, and E. Marsili, Int. J. Electrochem. Sci. **8**, 1778 (2013), available at http://www.electrochemsci.org/papers/vol8/80201778.pdf.
[46]B. Virdis, D. Millo, B. C. Donose, Y. Lu, D. J. Batstone, and J. O. Krömer, RSC Adv. **6**, 3650 (2016).
[47]K. Artyushkova, J. A. Cornejo, L. K. Ista, S. Babanova, C. Santoro, P. Atanassov, and A. J. Schuler, Biointerphases **10**, 019013 (2015).
[48]K. Guo, S. Freguia, P. G. Dennis, X. Chen, B. C. Donos, J. Keller, J. J. Gooding, and K. Rabaey, Environ. Sci. Technol. **47**, 7563 (2013).
[49]M. Santini, M. Guilizzoni, M. Lorenzi, P. Atanassov, E. Marsili, S. Fest-Santini, P. Cristiani, and C. Santoro, Biointerphases **10**, 031009 (2015).
[50]E. Blanchet, B. Erable, M.-L. De Solan, and A. Bergel, Electrochem. Commun. **66**, 38 (2016).
[51]C. Santoro, Y. Lei, B. Li, and P. Cristiani, Biochem. Eng. J. **62**, 8 (2012).
[52]H. Beyenal, Z. Lewandowski, and G. Harkin, Biofouling **20**, 1 (2004).
[53]J. E. McGregor, L. T. Staniewicz, S. E. Guthrie Neé Kirk, and A. M. Donald, Methods Mol. Biol. **931**, 493 (2012).
[54]M. Santini, J. Phys.: Conf. Ser. **655**, 1 (2015).
[55]M. Santini, M. Guilizzoni, S. Fest-Santini, and M. Lorenzi, Rev. Sci. Instrum. **86**, 023708 (2015).
[56]D. Millo, F. Harnisch, S. A. Patil, H. K. Ly, U. Schröder, and P. Hildebrandt, Angew. Chem. **50**, 2625 (2011).
[57]B. Virdis, D. Millo, B. C. Donose, and D. J. Batstone, PloS One **9**, e89918 (2014).
[58]A. Jain, G. Gazzola, A. Panzera, M. Zanoni, and E. Marsili, Electrochim. Acta **56**, 10776 (2011).
[59]S. L. McArthur, G. Mishra, and C. D. Easton, *Surface Analysis and Techniques in Biology* (Springer, New York, 2014), Chap. 2, pp. 9–36.
[60]K. Artyushkova and P. Atanassov, ChemPhysChem **14**, 2071 (2013).
[61]H. Beyenal, C. Donovan, Z. Lewandowski, and G. Harkin, J. Microbiol. Methods **59**, 395 (2004).
[62]L. Lewandowski and H. Beyenal, *Fundamentals of Biofilm Research*, 2nd ed. (CRC and International Publishing Switzerland, Boca Raton, London, New York, 2013).
[63]E. Paramonova, E. D. de Jong, B. P. Krom, H. C. van der Mei, H. J. Busscher, and P. K. Sharma, Appl. Environ. Microbiol. **73**, 7023 (2007).
[64]E. Marsili, D. B. Baron, I. D. Shikhare, D. Coursolle, J. A. Gralnick, and D. R. Bond, Proc. Natl. Acad. Sci. U. S. A. **105**, 3968 (2008).
[65]I. S. Chang, O. Bretschger, A. C. M. Cheung, F. Mansfeld, and K. H. Nealson, Electroanalysis **22**, 883 (2010).
[66]ThermoFisher Scientific BacLight Protocol, http://goo.gl/i9RiOB.
[67]K. Artyushkova, "Areal, volumetric and textural parameters from 2D and 3D images," 2014, http://goo.gl/CmbCk7.
[68]M. A. TerAvest and L. T. Angenent, ChemElectroChem **1**, 2000 (2014).
[69]D. Legland, K. Kiêu, and M.-F. Devaux, Image Anal. Stereol. **26**, 83 (2007).
[70]B. Kundukad, T. Seviour, Y. Liang, S. A. Rice, S. Kjelleberg, and P. S. Doyle, Soft Matter **12**, 5718 (2016).